NO($X\,^2\Pi$) product state distributions in molecule–surface collision-induced dissociation: Direct inelastic scattering of *n,i*-C_3F_7NO from MgO(100) at $E_{incident} \leqslant 7.0$ eV

E. Kolodney,[a] P. S. Powers,[b] L. Hodgson,[c] H. Reisler, and C. Wittig
Department of Chemistry, University of Southern California, Los Angeles, California 90089-0482

(Received 8 December 1989; accepted 24 September 1990)

Molecule–surface collision-induced dissociation (CID) has been studied for *n*-C_3F_7NO and *i*-C_3F_7NO molecular beams scattered from MgO(100) at incident kinetic energies ($E_{incident}$) up to 7 eV. The NO fragment was detected state selectively using two-photon, two-frequency ionization, and rotational and spin–orbit distributions are reported for several $E_{incident}$ values. State and angle-resolved signals were integrated to give CID yields, which increased sharply with $E_{incident}$. In most cases, rotational excitation could be described by separate temperatures for each spin–orbit state. The upper $^2\Pi_{3/2}$ state was underpopulated relative to statistical predictions (e.g., for *n*-C_3F_7NO at $E_{incident} = 5.0$ eV, the spin–orbit temperature was ~ 170 K, while T_{rot} was ~ 500 K). The CID results are compared to NO state distributions derived from the photodissociation of expansion-cooled molecules under collision-free conditions, at different energies ($E^\dagger$) above D_0. These distributions were measured for both *n*-C_3F_7NO and *i*-C_3F_7NO up to $E^\dagger \sim 4500\ cm^{-1}$, and rotational excitation within each spin–orbit state was statistical, except at $E^\dagger \geqslant 3000\ cm^{-1}$. As with CID, a low $[^2\Pi_{3/2}]/[^2\Pi_{1/2}]$ ratio was observed, and the reaction mechanism is probably unimolecular decomposition via the lowest triplet surface T_1 with little or no exit channel barrier. The pronounced similarities between the CID and photodissociation results suggest that common reaction mechanisms *may* be operative. All of the CID results are compatible with direct inelastic scattering followed by unimolecular reaction on the S_0 and/or T_1 potential surfaces.

I. INTRODUCTION

During the last decade, there has been growing interest in hyperthermal (1–20 eV) atomic and molecular beam scattering from single-crystal surfaces. This energy range is important because it encompasses bond dissociation energies, activation energies for chemical reactions, and threshold regions for efficient coupling of incident kinetic energy, $E_{incident}$, to intramolecular and crystal excitations. Thus, understanding the microscopic dynamics that govern such interactions is of both scientific and technological interest.

Most of the experimental work reported to date in this area has involved direct inelastic scattering (i.e., from the steeply repulsive part of the molecule–surface potential) of atoms and diatomic molecules from metal, insulator, and semiconductor surfaces.[1-12] Relatively few studies have been concerned with collisional excitation and dissociation of *polyatomic* molecules following impulsive impact on single crystals.[13] The gaseous counterparts of these processes, especially collision-induced dissociation (CID) of molecular ions, are known to have significant cross sections that rise rapidly with $E_{incident}$.[14,15] The observed thresholds for these reactions are close to the lowest bond energies, with cross sections sometimes reaching saturation near the hard sphere values for center-of-mass (c.m.) collision energies less than 10 eV. Since in gas-phase collisions efficient vibrational excitation takes place at c.m. collision energies of only a few eV, it is expected that comparable distortions of the molecular frame would occur in collisions of molecules with stiff surfaces.

In a pioneering series of experiments, Amirav and coworkers reported high CID efficiencies via direct inelastic scattering of molecular beams of I_2 and C_3H_7I from stiff, chemically inert single crystals [MgO(100), Al_2O_3(0001), diamond (111)] at $E_{incident}$ values of 2–10 eV.[16-18] These studies show that molecule–surface excitation and CID can be important even at modest collision energies. Such beam–surface studies offer several advantages over their gas-phase molecular ion counterparts: (i) Parent molecules can be cooled in supersonic expansions, and $E_{rot} < 10$ K and modest E_{vib} can be easily achieved, while surface excitations can be controlled by varying the type of crystal and its temperature. (ii) The collision probability with the surface is unity, much higher than in gas-phase reactions (which are usually carried out in the single-collision regime), providing the requisite S/N for obtaining fragment angular and TOF distributions. (iii) The $E_{incident}$ spread of hyperthermal molecular beams prepared via supersonic expansion is fairly narrow, typically $\pm$ 10%, further defining and controlling the available energy.

In discussing possible CID mechanisms, insight can be gained from the gas-phase studies of molecular ions. In many cases, fragmentation of the energized molecular ions can be described by statistical unimolecular reaction theories, such as RRKM/QET.[14,15] Thus, for molecules or molecular ions with many degrees of freedom, unimolecular decomposition rates at internal energies slightly in excess of D_0 can be rather slow, much slower than the initial collisional activation step, and increase rapidly with energy. The

[a] Chaim Weizmann postdoctoral fellow; present address: Chemistry Department, Technion Institute of Technology, Haifa, Israel.
[b] Dept. of Education fellow.
[c] NSF predoctoral fellow.

 0021-9606/91/032330-16$03.00

nature of the activation process itself is less clear, and key issues, such as the fraction of the translational energy converted to E_{internal} per collision, and its dependence on the collision energy and the nature of the target, remain open. Although the duration of the activation collision is usually too short to allow molecule–target complex formation with full energy randomization, a mechanism involving collision-induced coupling of at least some of the incident molecule and target degrees of freedom appears to give a fair qualitative description of the collisional activation step in molecular ions.[15] Thus, although it is thought that perhaps not all degrees of freedom are accessed directly in the collision, the subsequent fragmentation of the energized molecular ions can be described by RRKM/QET.

In molecule–surface collisions at $E_{\text{incident}} < 20$ eV, several additional and complementary mechanisms have been invoked. The CID of I_2 has been modeled with a mechanism involving a high torque acquired in the molecule–surface collision, followed by dissociation of the rotationally excited molecules. Vibrational excitation was found to be relatively inefficient in diatomic–surface collisions.[17] However, for large polyatomic molecules, vibrational excitation has been observed following molecule–surface collision, and is expected to be an important mechanism.[19] Another mechanism, proposed by Gadzuk and co-workers,[20] involves molecule–surface charge transfer with the formation of transient ions, leading to vibrational excitation of the scattered molecule. Such a mechanism may be important in metals and semiconductors, but its relevance to CID on insulators such as MgO has not been demonstrated.[20]

Experimental observations in molecule–surface hyperthermal collisions include: (i) detection of both positive and negative fragment and molecular ions with efficiencies as high as 0.1%;[18] (ii) efficient energy transfer to crystal excitations [e.g., $I_2 + MgO(100)$];[1,2] (iii) dependence of the CID probability on the nature of the surface;[13,16,17] (iv) dependence of the CID probability on the incident molecule [e.g., in collisions with diamond (111), CID probabilities increase in the order $CH_3I < C_3H_7I < C_6H_{13}I$ for comparable collision energies];[13] (v) weak fluorescence from an electronically excited fragment ($\sim 2\times10^{-7}$ photons molecule^{-1}) following collisional activation on various organic surfaces;[21] and (vi) collision-induced dissociation and desorption of adsorbed species energized by high E_{incident} atoms.[22]

With the hope of further sorting out the mechanisms important in molecule–surface CID, we report here studies in which fragment quantum-state distributions are obtained, in addition to measuring the variation of CID yields with E_{incident}. Product state distributions are particularly useful in identifying statistical mechanisms (i.e., unimolecular decomposition), and deviations from statistical behavior can be revealed by comparisons with the predictions of well-established theories (e.g., RRKM, prior). In addition, we envision exploiting the method as a general means of activating large polyatomic molecules under well-controlled conditions, in order to study their decomposition pathways and mechanisms. It was with this perspective that we carried out the first CID experiments in which state-resolved reaction products were detected.[23] The present paper contains a complete description of these experiments, including an extensive data set, as well as a discussion of possible reaction mechanisms.

In the present set of experiments, we chose aliphatic nitroso molecules, RNO, since (i) they all have low D_0 values (< 2 eV),[24] (ii) the R species can be made heavy (e.g., perfluorination) to allow aerodynamic acceleration to $E_{\text{incident}} > D_0$, (iii) the NO fragment can be easily and sensitively detected by photoionization (10^{-12} Torr per quantum state is observed), and (iv) the gas-phase, $E^{\dagger}$-dependent unimolecular reactions of several isolated RNO molecules have been studied in detail, and were found to exhibit common features, which can be compared with molecule–surface CID results.[24] More specifically, in the work reported here, *n*- and *i*-C_3F_7NO were scattered from a MgO(100) single crystal surface at $E_{\text{incident}} \leqslant 7.0$ eV. The use of two isomers was motivated, in part, by a desire to identify molecule–surface orientation effects in CID. We report fully resolved NO internal state distributions, as well as CID yields vs E_{incident}. In a parallel series of experiments, we studied photoinitiated unimolecular reactions of the same molecules using expansion cooling and well-defined $E^{\dagger}$ values up to 4500 cm^{-1}. The possibility of using this detailed information as a comparative database is examined in a general discussion of possible CID mechanisms. Based on the similarities with the photoinitiated unimolecular reactions of nitroso molecules, we suggest that the CID of C_3F_7NO occurs via statistical dissociation in the gas phase following excitation by impact on the surface.

Although the paper follows a tradition format, the experimental section is very detailed. This is the first in a series of papers describing collisional excitation and dissociation in molecule–surface collisions, and some of the data processing requires approximations and assumptions. Thus, we deem it appropriate to present a complete description of methodologies and procedures. The reader who is not keen on such detail can move quickly to the results section, perusing the experimental section as necessary.

II. EXPERIMENTAL

A. Molecule–surface collision-induced dissociation

1. Experimental arrangement

A schematic diagram of the overall experimental arrangement is shown in Fig. 1. Briefly, it consists of a pulsed molecular beam source, a buffer chamber, an ultrahigh vacuum (UHV) surface scattering and characterization chamber, and state-selective detection based on two-photon, two-frequency laser ionization of NO. In what follows, detailed descriptions of the different components and experimental procedures are given.

A pulsed, supersonic molecular beam of *n,i*-heptafluoronitrosopropane (C_3F_7NO, Fluorochem) seeded in a H_2 or He carrier gas was skimmed and collimated in a two-stage differentially pumped region before it entered the main UHV chamber (base pressure $\sim 5\times10^{-10}$ Torr). The source chamber was pumped by a standard diffusion pump (Varian VHS-6), while the scattering chamber was pumped

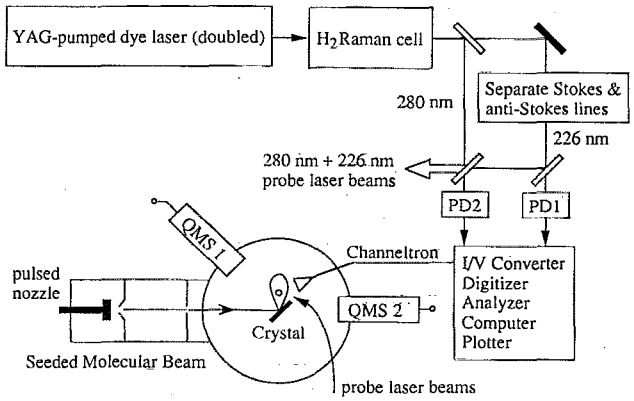

FIG. 1. Schematic drawing of the overall experimental arrangement used in the molecule–surface CID studies.

by a LN_2-trapped diffusion pump (Alcatel Crystal UHV 150). An auxiliary ion pump (Perkin Elmer 25) maintained the pressure overnight at 5×10^{-8} Torr. The UHV scattering and buffer chambers could be isolated from the nozzle source. The piezoelectrically driven pulsed valve (Lasertechnics) had a 0.5 mm nozzle aperture, but operated in a partially open mode due to the limited plunger movement. Based on total throughput measurements, this resulted in an effective opening diameter of $\sim$0.17 mm. Temporal pulse widths were typically 100–150 μs. These long pulse durations, as well as small velocity inhomogeneities in the leading and trailing edges of the beam, prevented accurate velocity measurements of the *scattered* beam. In order to quantify the velocity distribution of the incident beam under our experimental conditions, NO was seeded in a light carrier gas (e.g., 1% in He) and detected state selectivity at two points spaced 20 cm apart along the beam axis, i.e., in the center of the buffer chamber and 15 mm from the surface in the scattering chamber. By recording NO density profiles at these two points, with the laser tuned to the $Q_{11}+R_{21}$ bandhead ($0.5\leqslant J''\leqslant5.5$), the velocity distribution could be inferred quite accurately, and leading and trailing-edge effects were seen to be minor. In addition, the steep dependence of the CID probability on E_{incident} (see below) discriminates against lower velocities in the incident beam. We conclude that contributions from velocity inhomogeneities in the beam pulse are less than 10%, within the uncertainty of the E_{incident} measurements discussed below.

The pulsed valve was mounted on an XYZ translation stage, which could be manipulated from outside the vacuum. It could be resistively heated to 120 °C continuously under normal operating conditions, and heated intermittently to 160 °C using differential heating. The expansion was skimmed using thin electroformed nickel skimmers (Beam Dynamics, 0.8–1.5 mm orifices), and optimal nozzle–skimmer distances (typically 12–15 mm) depended on the skimmer orifice and nozzle throughput. The beam was further collimated by a 1.2×4.0 mm^2 slit as it entered the main scattering chamber.

The incident molecular beam was scattered from a cleaved, single crystal MgO(100) surface (Atomergic, $10\times10\times1$ mm^3). The geometries of the skimmer and slit resulted in a beam shape at the surface that could be approximated by a 1.6×6.0 mm^2 rectangle, meaningfully smaller than the effective (i.e., weighted by a cosine projection factor) surface dimensions of 7.5×10 mm^2. Note that the rectangular density profile approximately matched the effective ionization zone, since the probe laser was mildly focused (150 cm focal length lens), resulting in good depth of field. The crystal was x-ray analyzed in order to determine the plane and azimuthal directions prior to mounting. Once inside the UHV chamber, the crystal was annealed at 1100–1200 K for several hours. Fast Ar-atom bombardment (Ion Tech) was sometimes used to clean the surface before thermal annealing. The crystal holder was made of tantalum and molybdenum, and provided for resistive heating up to 1400 K.

These surface preparation and cleaning procedures resulted in reliable He diffraction patterns and a sharp, background-free Xe scattering angular distribution (16° FWHM at $E_{\text{incident}}=2.1$ eV), as shown in Fig. 2. Although the He diffraction pattern was superimposed on a substantial component of incoherent (diffusive) elastic background, as expected for cleaved surfaces,[25,26] Xe scattering was essentially background free, indicative of an atomically clean surface as seen by the physically large and heavy collider.[2] We investigated this effect in more detail, and found that Xe scattering at E_{incident} values of 1–5 eV was quite useful for characterizing surface dynamical conditions for collisions of heavy molecules with the surface. Direct inelastic scattering in the hyperthermal energy range, particularly the widths of the angular distributions, has been shown to yield valuable information about the effective surface corrugation and topography as a function of E_{incident}, as seen by the incoming particle.[1,4] Broadening is usually interpreted as the onset of increased corrugation (structure scattering).[4(b)] For ther-

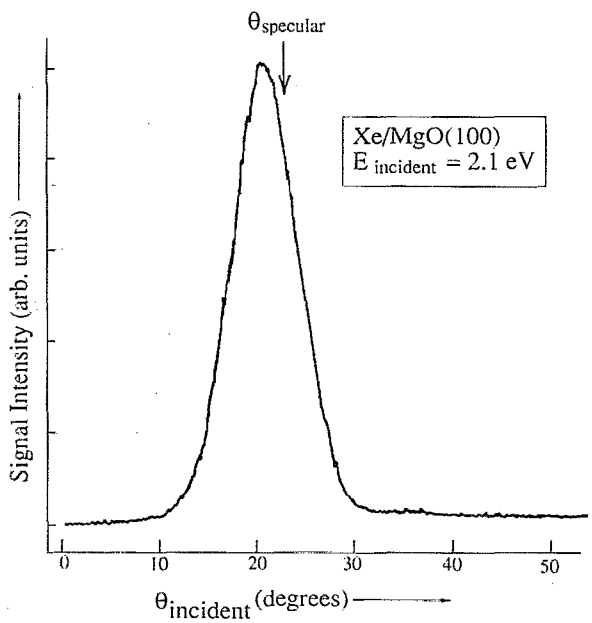

FIG. 2. Scattering of Xe atoms from MgO(100) at $E_{\text{incident}}=2.1$ eV. The beam–QMS 1 angle is fixed at 45° and the beam–surface angle is scanned by rotating the surface.

mal He atoms, the MgO(100) corrugation amplitude ζ_{10} is ~ 0.18 Å,[25,26] but is meaningfully less for bigger colliders like NO and Xe, as suggested by the widths of their scattering lobes.[9] Large atomic colliders (e.g., Ar, Xe, Hg), as compared with molecules, are particularly suited for these studies, since width changes in the angular distributions reflect the surface topography without the added complication of internal excitations encountered in molecules. In our case, for example, the angular scattering width narrows with increasing E_{incident} (e.g., 16° FWHM at 2.1 eV vs 12° FWHM at 3.6 eV) without any background contribution. This implies that the molecule–surface interaction potential for these systems at these energies is not highly corrugated, i.e., "chemical corrugation" effects are not important for the molecule/MgO system with its shallow interaction wells.

In order to ensure surface cleanliness (adsorbate-free and direct scattering conditions), the surface temperature T_s was maintained at 600 K during all experiments, except those in which T_s dependences were investigated. None of the results reported here depended strongly on temperature in the range 400–650 K, reflecting the direct inelastic nature of the scattering process, although preliminary measurements indicate that CID yields increase with T_s, particularly above 700 K. Details will be published elsewhere.

2. Detection systems—General

Throughout the experiments, two-photon, two-frequency laser ionization was used as the main probe, providing state-selective fragment distributions and beam diagnostics in the energy, time, and space domains. In addition, two quadrupole mass spectrometers (QMS's, UTI-100C) were used for measuring angular scattering distributions, time-of-flight (TOF) spectra, and relative intensities of the C_3F_7NO beams, as well as serving as residual gas analyzers. With the exception of the laser detection, the scattering/detection arrangement is that of fixed detectors and a rotating crystal. One QMS was oriented at 45° relative to the incident molecular beam, 26 cm from the surface, and was equipped with a collimator to give 1.1° resolution both in and out of the scattering plane. A second QMS was placed in-line with the incident molecular beam for diagnostics and E_{incident} measurements.

3. Laser photoionization detection

NO was detected state selectively using two-photon, two-frequency ionization via the $A\,^2\Sigma^+ \leftarrow X\,^2\Pi\ \gamma$ system. Several μJ of radiation near 226 nm and ~ 1 mJ of ionizing radiation near 280 nm resulted in a detection sensitivity of approximately 10^{-12} Torr per quantum state when using a 300 K NO static sample. The output from a 10 Hz Nd:YAG-laser pumped dye laser (Quanta-Ray DCR2/PD1) was doubled to give approximately 5 mJ of pulsed, tunable radiation near 280 nm. Part of this output was converted to ~ 226 nm using the second anti-Stokes line from a high pressure H_2 Raman scattering cell. It was then separated from the other Stokes and anti-Stokes components using two Pellin–Broca prisms in a mirror image configuration. Approximately 1 mJ of the 280 nm radiation was overlapped with the 226 nm radiation, providing two-frequency excitation. Both beams traveled similar path lengths between splitting and recombination, resulting in a temporal overlap better than ± 0.3 ns. When using $\sim 4\,\mu$J per pulse (in a 1 mm^2 beam) of tunable radiation in the 226 nm region to excite $\gamma(0\text{–}0)$ rotational transitions, and ~ 1 mJ near 280 nm to pump the ionizing transition, high S/N was achieved without even partially saturating the γ band. With the present conditions, 226 + 226 nm photoionization was less than 1% as efficient as 226 + 280 nm photoionization.

There are several distinct advantages to this two-frequency photoionization scheme, as opposed to using two 226 nm photons, as is typically done. Most are associated with the low intensities of the 226 nm radiation: (i) Due to improved Franck–Condon overlap,[27] the ionization cross section at 280 nm is larger than that at 226 nm. Moreover, since higher intensities are available near 280 nm, we achieved higher detection sensitivity while still avoiding even partial saturation of the NO γ-band transitions. This also avoids complications due to linewidth broadening (the 226 nm intensity is more than a factor of 10 smaller than the saturation limit). (ii) There are relatively few stray photoions and photoelectrons, probably caused by scattered 226 nm photons hitting the channeltron. The 280 nm radiation generates almost no photoions/photoelectrons—less than 1% yield relative to 226 nm photons. This enabled us to freely and accurately scan the photoionization point over all of the scattering plane, for a given surface angle, without compromising S/N. This was done by separately controlling the micrometer-driven translation stages of two 90° beam-turning quartz prisms (see Fig. 3). (iii) Because of the low 226 nm fluence, no dissociation of the parent molecule is detected, i.e., accounting for less than 2% of the scattered signal. This is significant, because the 226 nm $\pi^* \leftarrow \pi$ absorption cross section for perfluoronitroso alkane compounds is larger, by at least a factor of 50, than that at 280 nm ($\epsilon = 22.7$ attributed to a $\pi^* \leftarrow n$ transition).[28]

A schematic drawing showing how the laser beams enter and traverse the UHV chamber is given in Fig. 3. The 226 and 280 nm beams are made to propagate collinearly using a number of prisms, beam splitters, and irises mounted on a large optical table which is several meters from the vacuum system that holds the YAG-pumped-dye, doubling, Raman scattering, and frequency mixing assemblies. As shown in the figure, the probe beams travel vertically through the chamber, with x and y movements controlled outside the chamber.

As mentioned above, photodissociation in the incident beam was insignificant. This was checked in both the buffer and scattering chambers. However, in principle, it is possible that collision-induced internal excitation of parent molecules could markedly increase photodissociation and/or dissociative photoionization cross sections. Consequently, this was carefully checked by measuring the dependence of the signals on the 226 and 280 nm fluences. It should be pointed out that the inadvertent detection of NO as a *photodissociation product* [i.e., $\text{RNO} + h\nu(226\text{ nm}) \rightarrow \text{R} + \text{NO}(X\,^2\Pi)$, followed by $\text{NO}(X\,^2\Pi) + h\nu(226\text{ nm} + 280\text{ nm}) \rightarrow \text{NO}^+(X\,^1\Sigma^+) + e^-$] is a three-photon process, requir-

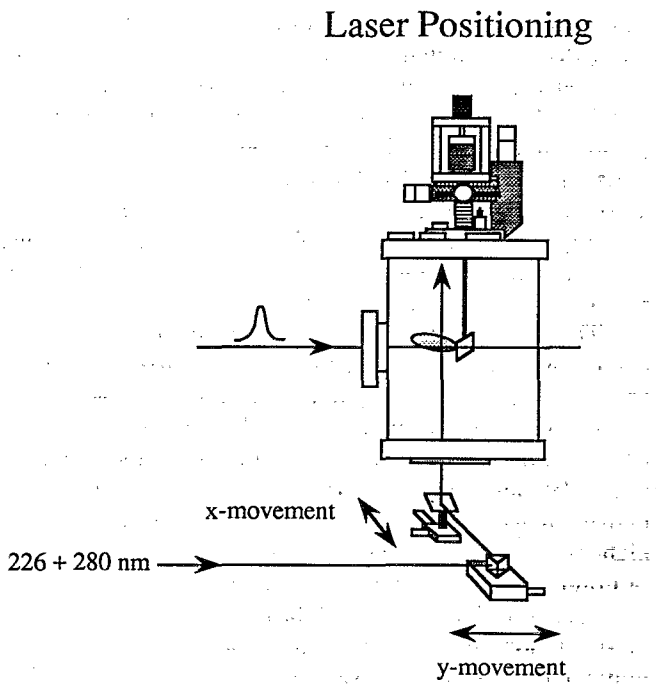

FIG. 3. Schematic drawing of the positioning of the laser beams relative to the crystal and incident and scattered molecular beams.

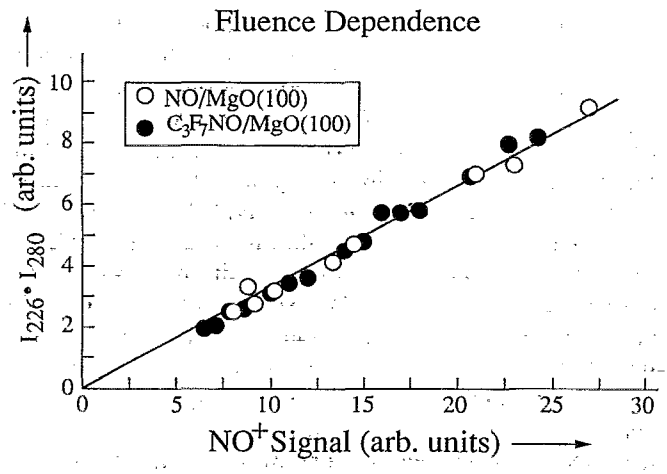

FIG. 4. NO signal detected at the $Q_{11} + R_{21}$ bandhead vs the $I_{226} \cdot I_{280}$ fluence product for an inelastically scattered reference NO beam (O) and CID (●); both are virtually identical. The linearity indicates that NO is not produced photolytically in the CID experiments.

ing two 226 nm photons, and its probability is therefore negligible under the present conditions. Experimental verification is presented in Fig. 4. To within $\pm 3\%$, all signals (i.e., from scattered NO as well as CID) were linearly proportional to the 226 and 280 nm fluences. These fluences were varied either independently (changing one while keeping the other constant), or simultaneously. The straight line shown in Fig. 4 was fixed at the origin and a "best fit" was obtained by visual inspection. No attempt was made to fit the data with a least-squares routine, since the distinction between two- and three-photon processes is clear.

As shown in Fig. 3, the overlapped, copropagating probe beams entered the main scattering chamber from the bottom through an 11 cm diameter sapphire window, crossing the scattering plane (defined by the molecular beam axis and the surface normal) at right angles, 14 mm from the surface. This resulted in an in-plane angular resolution of approximately 8° (2 mm laser beam width) and full integration out of the plane, i.e., along the long dimension of the rectangular scattered beam profile. For increased angular resolution, the laser beams were moved as much as 40 mm from the surface. Both probe beams were either collimated or mildly focused using a 150 cm focal length lens.

Ions were collected and detected using a channeltron (Galileo)–electrode arrangement, whose output was amplified and sent to a transient recorder (Nicolet) and computer system (LSI 11/23). Data processing included gated integration with dynamic base line subtraction, signal averaging (typically 10 shots per grating step at 10 Hz), and shot-to-shot normalization of the signals, using separate photodiodes to monitor the 226 and 280 nm energies. The product of the 226 and 280 nm photodiode signals (PD1 and PD2 in Fig. 1) served as the normalization factor. Rotational state distributions were measured by probing the γ band in the range 223.4–227.0 nm. Relative level densities N_J were extracted by dividing the normalized, integrated signal intensities by the appropriate line strengths (Hönl–London factors).[29] Only well-resolved and unambiguously assigned lines were used.

All measurements and procedures for extracting rotational distributions were checked routinely in the scattering chamber with 300 K NO samples using the same configuration as when detecting scattered species. Typical pressures ranged from 5×10^{-10} to 1×10^{-8} Torr. When plotted logarithmically, the ambient NO rotational distributions exhibited straight lines with slopes of 300 ± 15 K for both spin–orbit states, an integrated spin–orbit ratio $[^2\Pi_{3/2}]/[^2\Pi_{1/2}] = 0.56$, and equal Λ-doublet populations, as expected for a 300 K spectrum. This also ensured that the 280 nm ionizing step did not distort the relative spectral intensities.

4. Kinetic energy control

E_{incident} values of the heavy molecule were varied using aerodynamic acceleration with H_2 and He, as well as He/Ar and H_2/Ar mixtures. The seeded beam method provides a unique way of accelerating a heavy molecule to hyperthermal energies.[30,31] A small percentage of the heavy molecule is seeded in a light carrier, and in the absence of velocity slip (velocity difference) between the two species, the final kinetic energy obtained by the heavy molecule in a fully expanded beam is given by

$$E_{\text{incident}} = M/\langle m\rangle \int_0^{T_n} \langle C_p\rangle dT \cong (M/\langle m\rangle)\{\langle C_p\rangle T_n\}, \quad (1)$$

where T_n is the nozzle temperature, M is the mass of the heavy molecule, and $\langle m\rangle$ and $\langle C_p\rangle$ are the average mass and heat capacity of the gas mixture, respectively. From this relation, it is obvious that the energy of the heavy molecule can

be varied by controlling the average mass and/or the source temperature. Alternatively, the velocity slip between the heavy molecule and carrier gas can be controlled. Throughout these experiments, all three methods were used interchangeably. Typical dilution ratios in H_2 and He ranged between 1:300 and 1:600, and small velocity adjustments were achieved by also seeding Ar into the gas mixture. Nozzle heating was limited to 75 °C by C_3F_7NO thermal decomposition, i.e., ~10% dissociation at 95 °C. Thus, all E_{incident} values up to 6 eV were obtained with a room temperature nozzle. Note that E_{incident} refers only to the incident kinetic energy achieved by aerodynamic acceleration, even though the colliding molecules contain some vibrational excitation due to incomplete cooling in the expansion. Beam velocities were determined using TOF, measuring the time delay between the valve's electrical trigger and the peak of the gas pulse arriving at the center of the QMS ionizer, located 760 mm downstream from the nozzle orifice. Reliable measurements were essential due to considerable velocity slip in seeded beams with mass ratios as high as 100.[30]

The main problem in making accurate TOF measurements using the Lasertechnics pulsed valve was estimating the electromechanical response time. Since it was found that this depends on plunger amplitude and backing pressure, each TOF measurement was preceded by a set of calibration measurements with neat He and Ar beams for which the terminal supersonic velocities for 300 K expansions are known $[v_{\text{rms}} = (5kT/m)^{1/2}]$. Comparing the observed and calculated flight times of these inert gases, the valve's response could be extracted. Ion flight times through the QMS rods were calculated iteratively for each incident kinetic energy, and subtracted from the measured time delay.

As mentioned in Sec. II A 1, we also compared kinetic energies determined using this procedure with the more accurate laser TOF measurements, in which the full pulsed NO molecular beam contour was plotted by measuring the NO^+ photoionization signal vs the scanned valve-laser delay at two points, 20 cm apart, along the beam path. Good agreement between the two methods was found for different NO/H_2 mixtures.

5. Data acquisition and analysis

Relative and absolute CID yields, as well as percent NO contamination, were measured using the configuration shown schematically in Fig. 5. Figure 5(a) shows an NO reference beam (typically 1.6% NO in H_2, $E_{\text{incident}} = 0.90$ eV), and two detection positions: ionization of the incident beam 20 mm before the surface and ionization of the scattered beam 15 mm from the surface. NO was detected at the $Q_{11} + R_{21}$ bandhead ($0.5 \leqslant J'' \leqslant 5.5$) with a 1.0 cm^{-1} laser bandwidth. The $t = 0$ marker shown schematically in the figure was probably due to scattered 226 nm photons hitting the channeltron; its intensity provided internal calibration. It is unrelated to the firing of the pulsed valve and serves only as a timing (i.e., not sensitivity) calibration. The incident angle θ_1 was usually 40°, with detection near the specular angle. Figure 5(b) shows the same configuration for the seeded C_3F_7NO beam. The relative signal intensity at position 1 probed the NO contamination level. The CID signal at

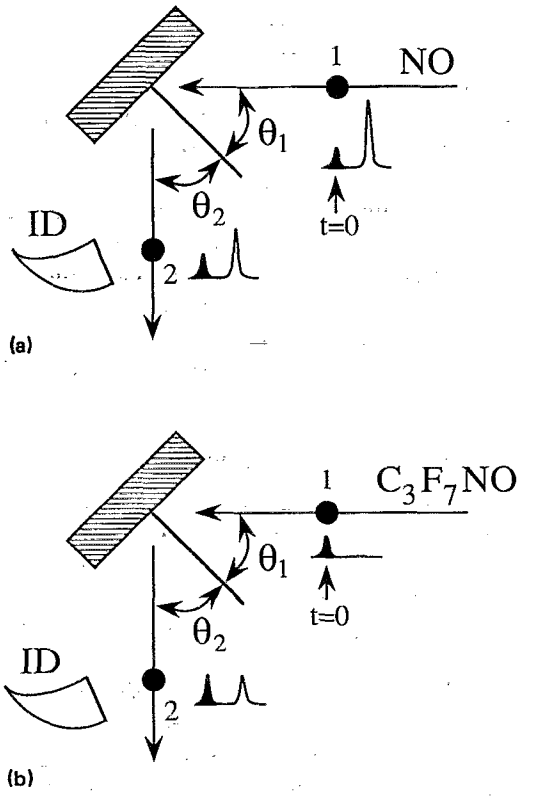

FIG. 5. Schematic drawing showing probe/surface configurations for (a) detecting scattered NO from an incident beam of known composition and (b) detecting NO from CID of C_3F_7NO [ID = ion detector (channeltron)]. The $t = 0$ pulse (darkened, artist's conception) appears concomitantly with the firing of the probe beams, and is probably due to photons striking the channeltron. It is unrelated to the firing of the pulsed valve and serves only as a timing (i.e., not sensitivity) calibration. These arrangements are used to estimate the CID yield as discussed in Sec. III.

position 2, relative to signals for other C_3F_7NO E_{incident} values and the signal from the NO reference beam, enabled us to determine relative and absolute CID yields as a function of E_{incident}. All measurements reported here were performed after maximizing the signal intensity as a function of the laser-valve delay time. NO internal state distributions were obtained at different laser-valve delays and did not change except at the edges of the gas pulse. Typically, 500–1000 laser shots were averaged in a single measurement. Procedures for converting photoionization signals to CID yields are discussed in Sec. III.

The NO contamination percentage in the incident C_3F_7NO beam and its relative contribution to the total scattered NO signal (i.e., CID + NO impurity) was determined using the incident-to-scattered intensity ratio for the NO reference beam as an experimental "transfer function" for both excitation and detection. The measurements included complete integration over rotational state distributions of (i) the incident NO beam (typically $T_R \approx 5$ K), (ii) scattered NO,[9] (iii) NO contamination in the incident C_3F_7NO beams (typically $T_R \approx 2$ K), and (iv) CID product NO. Partial integrations over angular scattering distributions were also carried out. This procedure allowed us to measure ratios of $[NO_{\text{fragment}}]/[C_3F_7NO_{\text{incident}}]$ of ~0.001 at $E_{\text{incident}} = 5.0$ eV. Care was taken to rid the gas manifold and pulsed valve

assembly of residual NO (i.e., below the detection limit) between the reference NO beam run and the C_3F_7NO beam run. In order to verify that NO is not backscattered from the surface and detected at position 1, we have repeated these measurements in the UHV chamber with the surface pulled away from the incident molecular beam line, as well as in the buffer chamber. Essentially identical results were obtained. Contamination level checks were performed routinely before and during each experiment. This was especially important when using a heated nozzle, in order to identify and quantify the onset of thermal decomposition. Typical contamination levels were only 2%–5% of the observed CID signal.

B. C_3F_7NO photodissociation experiments

The experimental arrangement used to study the collision-free one-photon photolysis of expansion-cooled *n,i*-C_3F_7NO has been described previously.[32] A pulsed nozzle (Lasertechnics, 0.5 mm diameter, $\sim 150\,\mu s$ pulse duration) was used to expand premixed He:C_3F_7NO samples (typically 500:2–5 Torr) into an LIF chamber which was maintained at $\sim 10^{-5}$ Torr. Photolysis was done using a YAG-pumped-dye system. A probe laser operating near 452 nm (Lambda Physik EMG 101 MSC excimer, FL 2001 dye), collinear and counterpropagating to the photolysis laser, was used to detect NO at variable delays following photolysis. The 452 nm output was frequency doubled with a BBO crystal (CSK Ltd.) to produce the 226 nm radiation necessary to probe the nascent NO fragments via one-photon laser-induced fluorescence (LIF) using the $A\,^2\Sigma^+ \leftarrow X\,^2\Pi$ γ system. Photofragment yield spectra were obtained by positioning the probe laser at the NO P_{11} bandhead ($7.5 \leqslant J'' \leqslant 10.5$) and scanning the photolysis laser. Room temperature C_3F_7NO absorption spectra were taken with a Shimadzu UV-visible spectrophotometer.

Samples of $\leqslant 1\%$ C_3F_7NO seeded in ~ 500 Torr He were prepared daily in a blackened glass bulb. C_3F_7NO was stored at 77 K and purified by trap-to-trap distillation to minimize NO contamination. Although NO could not be completely eliminated, expansion-cooled NO is limited to a few states (i.e., $^2\Pi_{1/2}$, $J'' \leqslant 4.5$). Care was taken to avoid this region when recording rotational distributions.

III. RESULTS

A. Collision-induced dissociation on MgO(100)

1. NO E, V, R excitations

A typical NO $A\,^2\Sigma^+ \leftarrow X\,^2\Pi$ spectrum deriving from molecule–surface CID is shown in Fig. 6(a) for an *n*-C_3F_7NO beam at $E_{\text{incident}} = 6.0$ eV. The other two panels show reference spectra obtained by scattering an NO beam at $E_{\text{incident}} = 0.9$ eV, and from ambient 300 K NO [Figs. 6(b) and 6(c), respectively]. All three spectra were normalized with respect to the laser energies and recorded using the same ionization point and detection configuration in the scattering chamber. Reference spectra were recorded and analyzed repeatedly during experiments as sensitive checks for small changes in detection or scattering configurations; these measurements were aided by our experience with

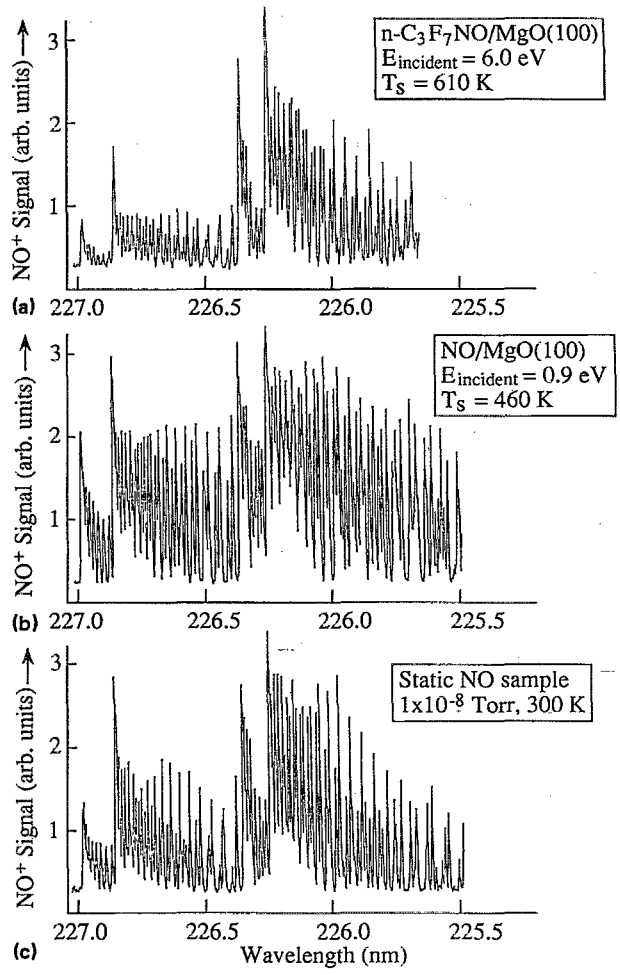

FIG. 6. NO $A\,^2\Sigma^+ \leftarrow X\,^2\Pi$ (0,0) spectra: (a) CID of *n*-C_3F_7NO, (b) scattered NO, (c) 300 K ambient NO. All spectra were recorded under identical conditions. The different rotational and spin–orbit excitations between the three spectra are easily seen.

NO/MgO(100) scattering under a variety of conditions.[9] When comparing the spectra, it is clear that the $[^2\Pi_{3/2}]/[^2\Pi_{1/2}]$ ratio obtained via CID is smaller than the corresponding ratios for scattered NO and 300 K NO.

Figures 7 and 8 show Boltzmann plots {i.e., $\ln[N(J'')/(2J''+1)]$ vs E_{rot}} of NO rotational distributions from the CID of *n*- and *i*-C_3F_7NO at several E_{incident} values, with $T_s = 600$ K and $\theta_i = 40°$ (see Fig. 5). These distributions were obtained by averaging results from 4 to 5 spectra. Rotational distributions obtained by averaging several rapid-scan spectra were preferred over those obtained from slow-scan spectra, even though the latter have higher S/N, as this avoids long-term drifts associated with changes of the surface, molecular beam, laser conditions, etc., thus minimizing systematic errors. Regardless, there was good agreement between results obtained from rapid and slow-scan spectra. Polarization effects were not pursued, since an isotropic $M_{J''}$ distribution is expected. The data presented in Figs. 6–9 were all obtained at the specular scattering angle.

As mentioned above, NO spin–orbit excitation from CID is low, $[^2\Pi_{3/2}]/[^2\Pi_{1/2}] = 0.36$, corresponding to a temperature of 170 K, and this ratio changes little with

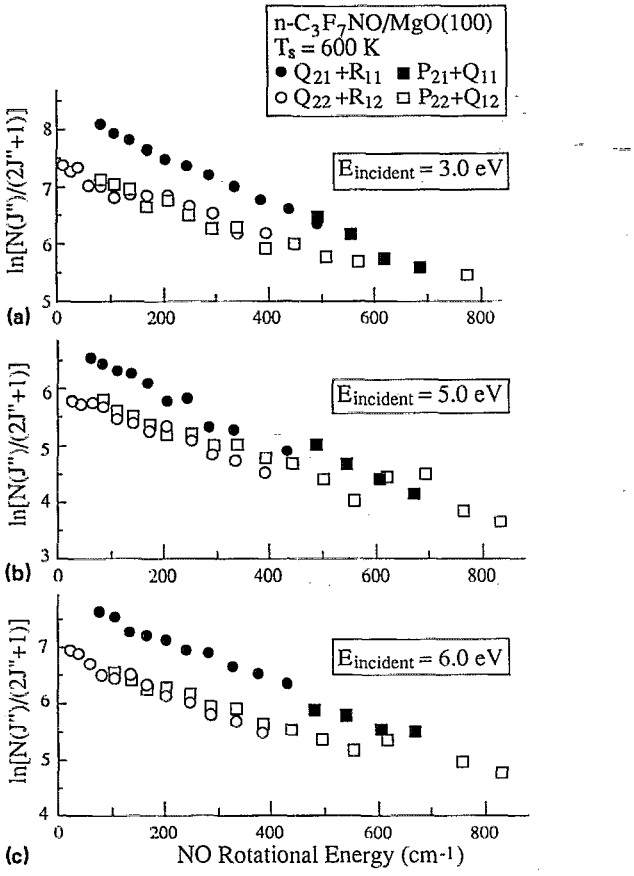

FIG. 7. Boltzmann plots of NO rotational distributions from n-C_3F_7NO CID at three $E_{incident}$ values and $T_s = 600 \pm 20$ K. Each distribution represents an average of several different measurements. The filled and empty symbols indicate rotational populations of $^2\Pi_{1/2}$ and $^2\Pi_{3/2}$ NO spin–orbit states, respectively.

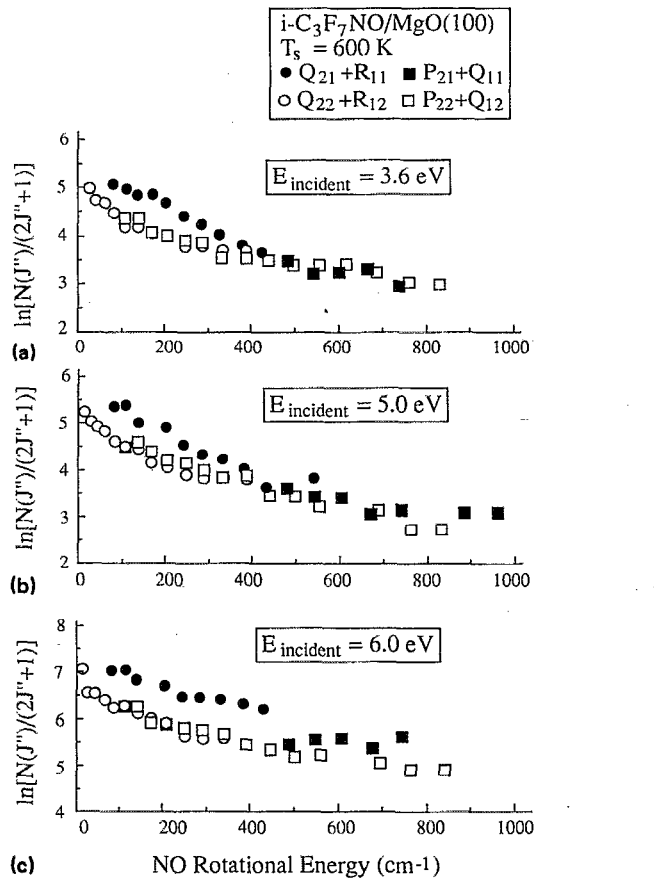

FIG. 8. Boltzmann plots of NO rotational distributions from i-C_3F_7NO CID at three $E_{incident}$ values and $T_s = 600 \pm 20$ K. Each distribution represents an average of several different measurements. The filled and empty symbols indicate rotational populations of $^2\Pi_{1/2}$ and $^2\Pi_{3/2}$ NO spin–orbit states, respectively.

$E_{incident}$. Were temperatures assigned to the rotational distributions, they would be several times higher. Note, however, that different rotational distributions were obtained for each spin–orbit state, with $^2\Pi_{3/2}$ consistently exhibiting higher rotational excitations. Although most of the distributions can be assigned temperatures, this is not always the case, and we generally avoid the use of temperatures, referring instead to the figures for estimates and comparisons of rotational excitations. Doing so may sacrifice brevity, but avoids the pitfalls of assigning single labels to distributions arising from a range of $E^\dagger$, and possibly involving several electronic states of the parent molecule. In general, NO rotational excitations were modest, and when straight lines could be drawn, $T_{rot} \sim 500$ K was usually obtained for $^2\Pi_{3/2}$, while T_{rot} in the range 350–420 K was obtained for $^2\Pi_{1/2}$.

The rotational distributions for both NO spin–orbit states produced by CID of n-C_3F_7NO appear Boltzmann-like, as shown in Fig. 7, although the upper $^2\Pi_{3/2}$ state has higher rotational excitation than $^2\Pi_{1/2}$ for all $E_{incident}$ values. The uncertainty in the rotational state populations is $\pm 6\%$. Note that, as expected for the low J'' probed, both Λ-doublet components were equally populated, since identical populations were derived from P/R and Q branches [i.e., $\Pi(A')$ and $\Pi(A'')$, respectively].[33] This can be seen in the $^2\Pi_{3/2}$ plots displayed in Figs. 7 and 8, where several branch lines were measured for each J''. Since the low J'' levels of NO are not expected to show Λ-doublet propensities, these measurements constitute a check of internal consistency.

Figure 9 shows the dependence of the NO state distributions on T_s in the range 420–770 K for n-C_3F_7NO at $E_{incident} = 5.0$ eV. The lower limit ensured that significant adsorption of C_3F_7NO on the surface did not occur during the course of an experiment, while at $T_s > 840$ K a strong ion background originating from the surface holder and heating filament interfered with the measurements. Figure 9 indicates that the rotational distributions depend weakly on T_s. T_{rot} for $^2\Pi_{1/2}$ is ~ 360 K, much lower than T_s. Only above 770 K do the $^2\Pi_{3/2}$ distributions show enhancements of high J''; e.g., around $J'' = 17.5$, as shown in Figs. 9(a) and 9(c). Experiments with i-C_3F_7NO at $T_s = 800$–870 K yielded similar distributions to that shown in Fig. 8 for $T_s = 600$ K. These results further demonstrate the direct inelastic nature of the scattering process, i.e., that NO is not being desorbed from the surface.

Several attempts were made to detect NO($v'' = 1$) from CID in the $\gamma(1,-1)$ region. However, no signal was observed with $E_{incident} = 5.0$ eV and $T_s = 600$ or 840 K. If we assume

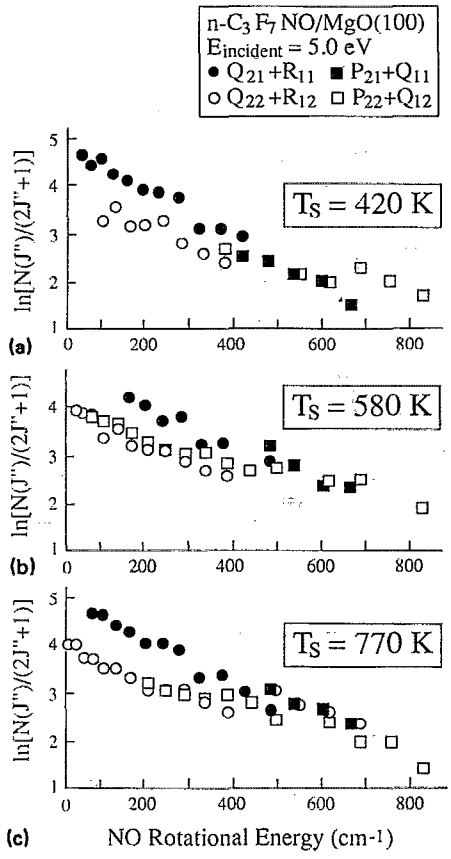

FIG. 9. Boltzmann plots of NO rotational distributions from n-C_3F_7NO CID at $E_{incident} = 5.0$ eV and three T_s values. Each distribution represents an average of several different measurements. The filled and empty symbols indicate rotational populations of $^2\Pi_{1/2}$ and $^2\Pi_{3/2}$ NO spin–orbit states, respectively.

similar spin–orbit and rotational distributions in $v'' = 0$ and 1, and take into account the different Franck–Condon factors, an estimated upper limit of 2% can be placed on the $[v'' = 1]/[v'' = 0]$ ratio. However, more detailed measurements are necessary in order to fully quantify NO vibrational excitation. $NO(v'' = 1)$ was observed previously in NO/Ag(111) direct inelastic scattering at high T_s,[11] and in NO/Pt foil and NO/Pt(111) photodesorption experiments.[34,35] In the case of NO/metal collisions, it was proposed that short-lived negative ion resonances were the source of vibrational excitation.[11] However, based on the electron affinities of NO (0.02 eV)[36] and C_3F_7 (2.3 eV),[36] and recalling that MgO is a good insulator, the formation of transient NO negative ions in the present experiments seems unlikely. As a further check on the possibility of direct vibrational excitation in collisions of NO with MgO(100) at high T_s, we scattered NO at $E_{incident} = 0.90$ eV and $T_s = 870$ K, but did not observe $v'' = 1$, thus placing an upper limit of 0.1% on the $[v'' = 1]/[v'' = 0]$ ratio. This should be compared with 4.5% vibrational excitation expected from accommodation with the 870 K surface.

2. Dissociation yields—Kinetic energy dependences

In what follows, "CID yield" refers to the NO fragment density, summed over internal states and scattering angles, *relative* to the corresponding signal from an NO reference beam, also summed over internal states and scattering angles. The incident C_3F_7NO beam flux is scaled to the incident NO reference beam flux, but product density/flux transformations are not carried out, as the scattered velocities are unknown (see Sec. IV). This prevents a direct experimental determination of the dissociation probability.[37] In addition, we do not assess the fraction of scattered molecules with $E_{internal} > D_0$ that pass through the detection region intact.

The variation of CID yield with $E_{incident}$ for n- and i-C_3F_7NO is presented in Fig. 10 for $T_s = 600$ K. As stated above, it is *densities* that are measured: internal-state specific, scattered into laboratory solid angle $d\Omega$, as a function of $E_{incident}$. Below, we describe procedures and assumptions involved in the analyses, deferring a discussion of systematic errors and biases to Sec. IV.

To determine *relative* CID yields at different $E_{incident}$ values, the following assumptions and procedures were adopted: (i) $NO(v'' = 0)$ internal states were summed for each $E_{incident}$; vibrational excitation was negligible and rotational distributions varied weakly with $E_{incident}$. (ii) NO state distributions and relative densities obtained over scattering angles or roughly 25°–45° (8° resolution) were similar. In addition, the same NO relative densities were obtained using a 5 mm probe diameter, i.e., 24° angular resolution. Both angular distributions were similar—broad and quasi-specular. Thus, we concluded that detailed angular integration is unnecessary. (iii) In determining relative CID yields, the incident C_3F_7NO flux was usually kept constant, with measurements at different $E_{incident}$ performed at a C_3F_7NO:H_2 ratio of 1:300, with final velocities adjusted by adding Ar or He while keeping the nozzle throughput constant. Relative incident fluxes were also determined in the scattering chamber by measuring relative C_3F_7NO signal in-

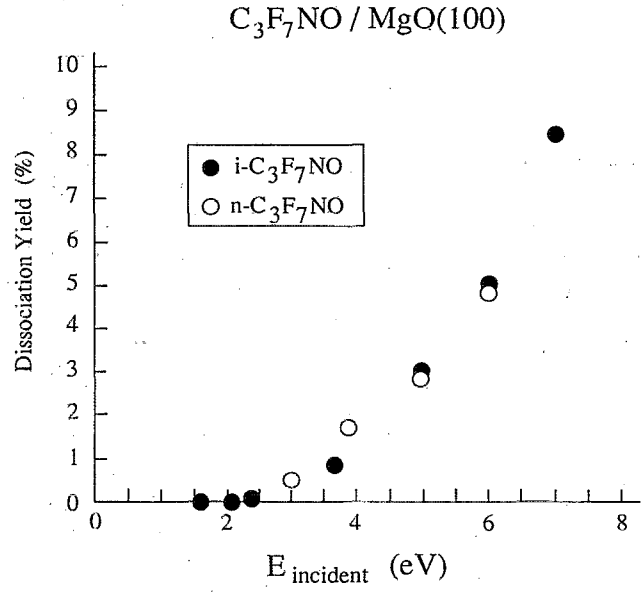

FIG. 10. CID yields for n-C_3F_7NO and i-C_3F_7NO vs $E_{incident}$ at $T_s = 600 \pm 20$ K. NO was monitored at the $Q_{11} + R_{21}$ bandhead. Uncertainty in absolute yields is ± 50%; relative values are ± 20%.

tensities with the QMS on the incident beam line. However, as a check, we also used gas mixtures with different amounts of C_3F_7NO (1:125 to 1:650) to achieve the same $E_{incident}$ values, and estimated the relative incident C_3F_7NO fluxes both from the nozzle throughput and by mass spectrometric determination, as described above. Good agreement between the two sets of measurements was obtained, and all CID yields fell nicely on a single curve. All the data points in Fig. 10, except the one at $E_{incident} = 7$ eV, were obtained with the nozzle at room temperature. (iv) Finally, we conclude that the variation of dissociation *probability* with $E_{incident}$ is probably steeper than the variation of dissociation yield shown in Fig. 10, as a result of the density/flux relationship. The uncertainty in the relative CID yields is estimated to be $\pm$ 20%.

In estimating *absolute* CID yields, a reference NO beam with well-controlled incident flux was used for calibration. This flux was either equal to the incoming C_3F_7NO flux or in a well-known ratio. Aerodynamic focusing (far-field enrichment of the beam center with the heavy molecule) was estimated experimentally by comparing incident beam flux ratios in the source and scattering chambers, and approximate enrichment ratios for C_3F_7NO seeded beams with respect to the NO reference beam were obtained. The extent of the effect depends strongly on specific apparatus parameters (e.g., nozzle–skimmer configuration and geometry, backing pressure).[38] In the calibration measurements, the NO and C_3F_7NO relative incident fluxes were measured both in the source chamber and in the scattering chambers. The NO photoionization signals from the scattered NO beam and the fragment NO from the CID experiments were then compared, with all other experimental parameters held constant (laser excitation conditions, surface parameters, detection, etc.). As described above, complete integration over the NO internal state distributions and partial integration over angular scattering distributions were performed for both beams, but density/flux transformations were not done. Calibration measurements were performed separately for each $E_{incident}$, rather than using just one value, as this provides a consistency check of the variation of relative CID yield vs $E_{incident}$, without compromising the better precision of the relative measurements. All CID yields represent an average of data taken over an extended period of time. The estimated uncertainty in the absolute yields is $\pm$ 50%.

Several important features are immediately apparent from Fig. 10. CID yield depends strongly on $E_{incident}$, reflecting the direct inelastic nature of the scattering event, with the data points for both *n*- and *i*-C_3F_7NO falling on the same curve. The apparent threshold for the CID of *i*-C_3F_7NO at $T_s = 600$ K was measured at 2.35 ± 0.20 eV ($D_0 = 1.69$ eV for *n*-$C_3F_7NO \rightarrow$ *n*-C_3F_7 + NO, and 1.64 eV for *i*-$C_3F_7NO \rightarrow$ *i*-C_3F_7 + NO), and from Fig. 10, a similar value can be inferred for *n*-C_3F_7NO. We assume that C_3F_7NO fragmentation occurs in the gas phase, where C_3F_7 + NO is the lowest energy channel, rather than on the surface. This "threshold" depends on experimental sensitivity, and presently corresponds to a CID yield of 0.1%. In these experiments, θ_1 was $37 \pm 2°$, and the probe beams were near the specular angle. As described above, the results represent, to a good approximation, an average over scattering angles in the range of 25°–45°.

B. Photodissociation results

Both *n*-C_3F_7NO and *i*-C_3F_7NO display prominent visible and near-IR $\pi^* \leftarrow n$ absorptions characteristic of RNO molecules.[28] Room temperature absorption spectra ($\epsilon_{max} = 22.7$)[28(a)] showing barely resolvable structure are presented in Fig. 11, along with NO fragment yield spectra obtained using expansion-cooled samples. With *i*-C_3F_7NO, the yield spectrum seems to follow the 300 K absorption profile, turning on near 680 nm, at the rising edge of the $\pi^* \leftarrow n$ system, but exhibiting sharper structural features than the corresponding bumps in the 300 K absorption spectrum, as expected for rotationally cold parent molecules. In contrast, NO yield spectra obtained using *n*-C_3F_7NO show a marked *increase* in signal with decreasing photolysis wavelength in a part of the spectrum where the room temperature absorption is *decreasing* with decreasing photolysis wavelength. Unlike *i*-C_3F_7NO, the NO yield is negligible where the $\pi^* \leftarrow n$ absorption is strongest, rising sharply only at wavelengths below ~650 nm. Since the dissociation threshold is at 731 nm (*vide infra*), and S_1 decays nonradiatively (i.e., there is essentially no parent fluorescence), this indicates that *n*-C_3F_7NO molecules just above D_0 do not disso-

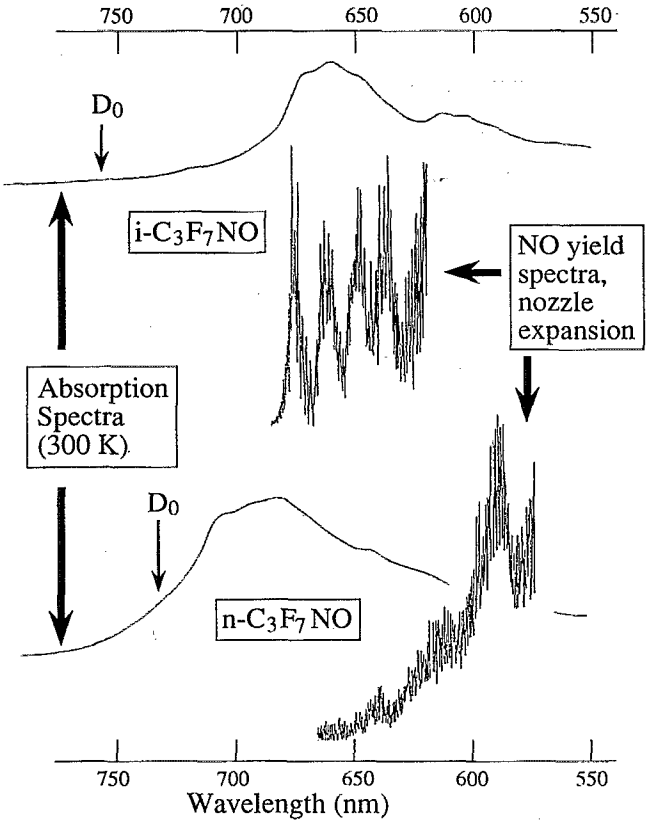

FIG. 11. Room temperature absorption spectra and expansion-cooled NO photofragment yield spectra for *i*-C_3F_7NO and *n*-C_3F_7NO. The NO was monitored at the P_{11} bandhead ($7.5 \leqslant J'' \leqslant 10.5$) while scanning the photolysis laser and the delay between the photolysis and probe lasers was 200 ns.

ciate within the pump–probe delays used in these measurements ($\leqslant 1\ \mu s$).

NO internal state distributions were obtained at several values of $E^\dagger$ for both *n*- and *i*-C_3F_7NO, as shown in Figs. 12 and 13, respectively. NO($X\ ^2\Pi$) is produced predominantly in $v'' = 0$ ($< 1\%$ in $v'' = 1$). An upper limit for D_0 was obtained from the highest observed J'' level in the long tail of the rotational distribution. Another estimate of D_0 was obtained by noting that the NO rotational distributions following dissociation at long wavelengths appear statistical. By fitting them with prior distributions using $E^\dagger$ as the single adjustable parameter, D_0 could be obtained. The values obtained by the two methods were very similar: $13\,200 \pm 100$ cm^{-1} for *i*-C_3F_7NO and $13\,670 \pm 100$ cm^{-1} for *n*-C_3F_7NO. These values are typical of alkyl nitroso compounds.[24] The solid lines in Figs. 12 and 13 correspond to the calculated statistical distributions (priors) of product excitations at fixed $E^\dagger$ values.[37] In the prior calculations, the vibrational frequencies of the parent molecules were obtained from the literature,[39] and the densities of states were estimated by using the Whitten–Rabinovitch approximation.[40] In addition, the prior distributions for each spin–orbit state were separately normalized to the data and the experimental relative spin–orbit populations are as shown in the figures. We find, as is common with other nitroso molecules, that although the rotational populations of each of the spin–orbit states is statistical, the spin–orbit ratio is colder than statistical. The remarkably good fit, with the exception of the higher excess energies, is consistent with previous results, in which S_0 and/or T_1 were implicated as the reactive surfaces, following radiationless decay of S_1.[24,41] Notice, however, that at high $E^\dagger$ deviations from statistical behavior occur. In particular, for *n*-C_3F_7NO the NO($^2\Pi_{3/2}$) rotational excitations at $E^\dagger > \sim 2000$ cm^{-1} greatly exceed the predictions of the prior calculations.

With *i*-C_3F_7NO, the lowest accessible $E^\dagger$ values were ~ 1500 cm^{-1} limited most probably by the $\pi^* \leftarrow n$ absorption profile. The NO appearance times were less than 200 ns in all cases, dropping slightly with increasing $E^\dagger$ to values ~ 100 ns near $E^\dagger$ values of 4500 cm^{-1}. Likewise, with *n*-C_3F_7NO, the NO appearance times were shorter than 1 μs. These short lifetimes are consistent with dissociation on T_1, since RRKM calculations[42] suggest that, in the absence of exit channel barriers, T_1 reaction rates are much larger than those for S_0 at the same energies. Thus, we conclude that the observed NO fragments are due to dissociation via T_1. Note also that NO was not observed at wavelengths greater than ~ 650 nm, even though the parent molecules absorb significantly at these wavelengths. This is consistent with *n*-C_3F_7NO dissociating on S_0, where long unimolecular decay times preclude the possibility of reaction on a time scale $\leqslant 1$ μs. Therefore, dissociation on S_0 is a "dark" channel in the photodissociation experiments. This interpretation is supported by the finding that the NO photofragment yields obtained in *n*- and *i*-C_3F_7NO photodissociation are much lower than those for CF_3NO, where dissociation on S_0 is fast ($< 1\ \mu s$).[43]

IV. DISCUSSION

The experimental results presented above are the first of their kind, in that state-resolved fragment internal excitations are observed, with good angular resolution, following molecule–surface CID. Two immediate benefits of such high precision are (i) no ambiguity about the species being detected, as opposed to mass spectrometric detection of scattered species, where it may not be possible to distinguish highly vibrationally excited parent molecules from neutral

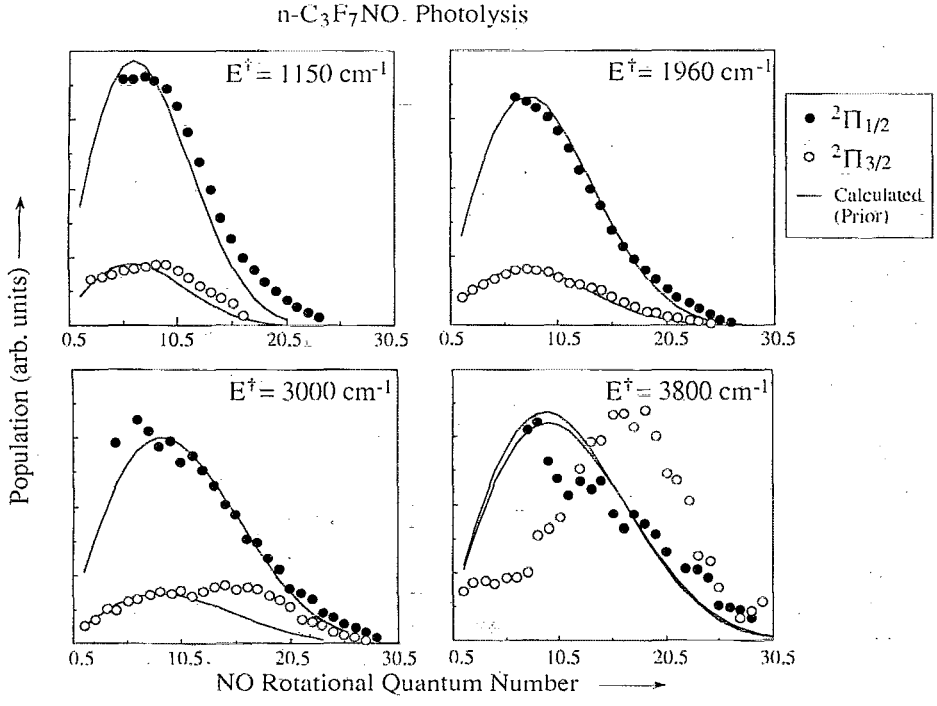

FIG. 12. NO state distributions from *n*-C_3F_7NO photolysis at various $E^\dagger$. The circles are data and the solid lines are statistical (prior) distributions. Rotational distributions are statistical at low $E^\dagger$ and show deviations at higher $E^\dagger$.

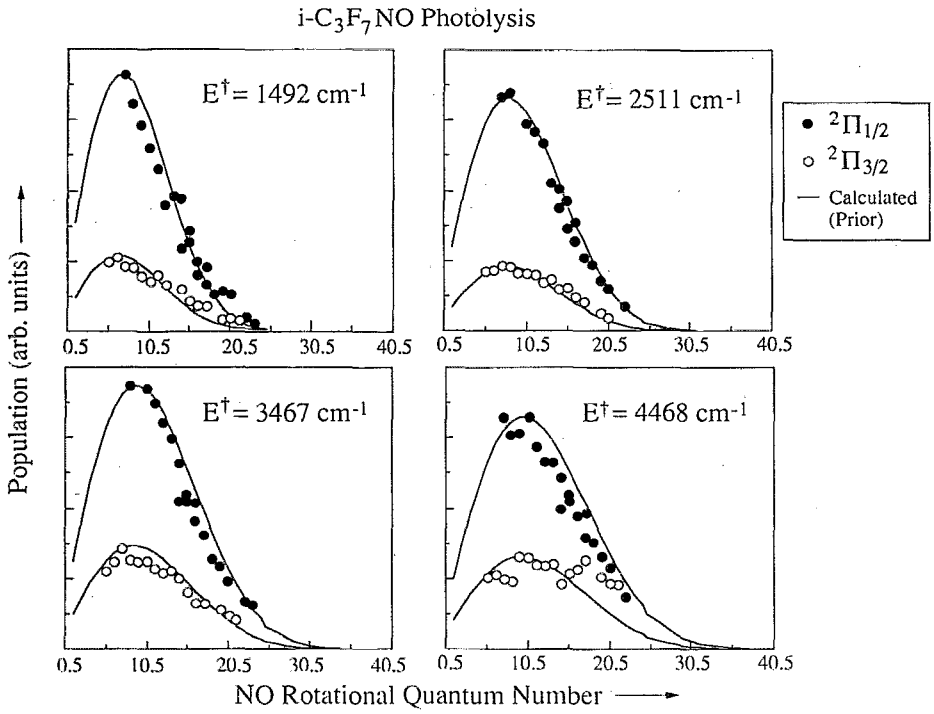

FIG. 13. NO state distributions from *i*-C_3F_7NO photolysis at various $E^\dagger$. The circles are data and the solid lines are statistical (prior) distributions. Rotational distributions are statistical at low $E^\dagger$ and show deviations at higher $E^\dagger$.

fragments, and (ii) the opportunity to infer mechanistic details from state-resolved observations of reaction products. Following collision with the surface, molecules rebound impulsively, and the collisional excitation process is direct inelastic in nature, as evidenced by the experimental observations: steep dependence of the CID yield on E_{incident}, absence of NO($v'' = 1$) even at high T_s, very weak dependence of the rotational distributions on T_s, and broad, quasispecular angular distributions.

In examining mechanisms that might rationalize the experimental observations, we considered: (a) direct bond rupture caused by strong collisional distortion of the C–NO bond upon impact, a rapid process that could be efficient for certain approach geometries, (b) dissociation following molecule–surface charge transfer processes, as inferred in previous hyperthermal surface scattering experiments,[13,18] and treated theoretically in terms of surface harpooning and the formation of temporary induced ions,[20] and (c) vibrational excitation within the S_0 and/or T_1 manifolds, followed by intramolecular vibrational redistribution and statistical unimolecular decomposition. With (a), the very similar variations of CID yield with E_{incident} for the iso and normal isomers do not support a strongly orientation-dependent excitation mechanism. Furthermore, if we assume that a head-on collision with the NO moiety of C_3F_7NO is required for violent bending of the C–NO bond, then to reconcile the highest fragment densities observed, near-unity dissociation probabilities are required for a roughly 47° cone about the surface normal, for those incident molecules having favorable orientations. Thus, we conclude that this is probably not a dominant dissociation mechanism.

With regard to mechanism (b), the study most closely related to ours is that of C_3H_7I scattered from diamond(111), where comparable CID yields were found, as well as positive and negative fragment ions, and collision-induced electronic excitation and/or dissociative ionization were suggested.[13] However, diamond is much stiffer than MgO, as evidenced by a bulk Debye temperature that is 2.3 times higher than that of MgO.[44] Also, oxide ceramics like MgO are excellent electrical insulators, and total positive ion yields in our experiments were less than 10^{-8} ions per incident C_3F_7NO molecule.[45] Thus, we are less inclined to invoke entrance channel charge transfer as the dominant mechanism than the intramolecular motions, distortions, and couplings that occur during the molecule–surface collision. Certainly, the situation can be different for metals and semiconductors, but for an insulator such as MgO, we envision a mainly repulsive molecule–surface interaction at the high E_{incident} values reported here.

The corrugation amplitude for thermal He scattering is larger for MgO(100) ($\zeta_{10} = 0.18$ Å)[25,26] than diamond (111) ($\zeta_{10} = 0.02$ Å).[46] However, one would expect that for colliders as big as molecules having 11 or 12 atoms, corrugation effects, although possibly playing some role, will be averaged out quite effectively and will not be dominant. Of course, this may not be true in cases in which molecular excitation is governed by local forces, e.g., around the NO group.

Thus, mechanism (c) is favored, and experimental evidence is presented below that supports this choice. However, we first discuss some of the experimental difficulties involved in the measurements.

A. Detection biases and systematic errors

As mentioned above, state-selective product detection (i.e., LIF or MPI) offers unique advantages and opportunities. However, there are also caveats imposed by the measurement of fragment level *densities*, rather than fluxes, and the relatively long dissociation time for molecules with low $E^{\dagger}$. Difficulties are due mainly to the connections between measured observables and fundamental quantities, such as the reaction probabilities into specific product states and the different velocity distributions associated with NO fragments with different internal states.

The decomposition of a molecule that has rebounded from the surface with $E_{\text{internal}} > D_0$ sends fragments recoiling into many angles in the molecule-based c.m. system. Given the nature of the overall fragmentation event, it is unlikely that products are scattered anisotropically in the c.m. system. However, the rebounding c.m. system moves anisotropically in the lab, with ranges of speeds and angles that depend on E_{incident}, θ_1, T_s, etc. Consequently, fragments may travel in many laboratory directions, but with velocity distributions that are difficult to anticipate.

Since it is relative fragment *densities* that are measured, several factors that involve flux/density transformations should be considered when interpreting the observed CID yields and state distributions. In general, rebounding molecules have less translational energy than when these same molecules were incident. This acts to increase the spatial density of such molecules, and the effect may be significant. For example, consider the case of $E_{\text{incident}} = 3.0$ eV. Rebounding molecules with $E_{\text{internal}} = D_0 + E^{\dagger} \sim 2.0$ eV have *maximum* translational energies around 1.0 eV (assuming $E_{\text{internal}} \sim 0$ for incident molecules), and most such rebounding molecules probably have translational energies below this value, since the MgO crystal receives some excitation. Thus, $E_{\text{rebound}}/E_{\text{incident}} < 1/3$, with a corresponding speed ratio $v_{\text{rebound}}/v_{\text{incident}} < 0.58$. Clearly, the density in the scattered beam, particularly for molecules that go on to react, is enhanced by this bunching effect. Molecule–surface collisions will generally produce a range of $E^{\dagger}$, with the higher values probably corresponding to smaller E_{rebound}, so data such as those shown in Figs. 7 and 8 cannot be interpreted as straightforwardly as in photodissociation experiments.

This bias will also be meted out differently for molecules having different E_{incident} values, since $E_{\text{rebound}} = E_{\text{incident}} - (E_{\text{MgO}} + D_0 + E^{\dagger})$. For example, with $E_{\text{incident}} = 6.0$ eV and $D_0 + E^{\dagger} \sim 2$ eV, maximum rebound translational energies are ~ 4 eV. Even allowing for MgO excitation, this places E_{rebound} closer to E_{incident} than with $E_{\text{incident}} = 3.0$ eV. Furthermore, since the experiments yield *ranges* of values for E_{rebound}, E_{MgO}, and $E^{\dagger}$, it is not presently possible to determine the appropriate flux/density transformations. In Sec. III, we delineated the assumptions and integrations involved in estimating CID yields. Near threshold, relative CID *probabilities* are probably smaller than the corresponding *yields*, due to the bunching effect, which will be most severe in the threshold region. Thus, we believe that CID probabilities increase more rapidly with E_{incident} than the data shown in Fig. 10.

As mentioned above, $C_3F_7NO^{\dagger}$ decomposition scatters fragments into NO internal and translational states in the C_3F_7NO c.m. system, and flux/density transformations are needed to relate the measured NO state-resolved densities to the corresponding nascent rotational distributions. For example, $C_3F_7NO^{\dagger}$ decomposition at energy $E^{\dagger}$ produces NO in a number of internal states, each of which has a distribution of translational energies. These distributions may differ from one NO state to the next (e.g., high J'' may be associated with lower c.m. translational energies), and this could result in a bias that favors detection of high J''. Thus, if the state-specific translational energy distributions *are* different, data analyses must account for this.

Another issue that needs consideration is that of effects associated with the finite and different $C_3F_7NO^{\dagger}$ unimolecular decay rates on T_1 and S_0. Molecules above reaction threshold on T_1 dissociate rapidly (i.e., on a time scale under a few hundred ns), so it is certain that no such molecules pass the detection region intact. In fact, on the macroscopic scale of experimental dimensions, fragments that accrue via T_1 essentially emanate from the surface, peaking around the specular angle. However, $C_3F_7NO^{\dagger}$ molecules dissociating on S_0 at comparable energies react much more slowly, with molecules at sufficiently low $E^{\dagger}$ actually having unimolecular decay rates $< 10^5$ s^{-1}. Thus, it is probable that some molecules, although excited above D_0, only dissociate after passing the detection region, which was typically 14 mm from the surface. For example, even for a modest v_{rebound} value of 10^5 cm s^{-1}, approximately 30% of the $C_3F_7NO^{\dagger}$ will pass through the detection region intact at $k_{\text{uni}} = 10^5$ s^{-1}. We presently have no way to assess this effect, which is important especially for molecules with low $E^{\dagger}$, but are optimistic that a fast chopper wheel (i.e., providing 2–3 μs pulses) will enable meaningful TOF measurements to be made in the near future.

In summary, the largest systematic errors and biases in our measurements derive from flux/density transformations and differences in unimolecular reaction times for molecules dissociating on different electronic surfaces and with a range of $E^{\dagger}$. These effects are most severe near D_0, particularly for molecules dissociating slowly on S_0, which may pass intact through the detection region. However, the enhancement in CID yield for E_{incident} near D_0, due to the bunching effect, may be somewhat offset by our inability to detect fragments from molecules dissociating on S_0 with low $E^{\dagger}$. The importance of such biases decreases with increasing E_{incident}. The qualitative considerations presented above suggest that the strongest biases affect the CID yields near threshold. The biases affecting the NO rotational distributions favor detection of high J'', but should not affect significantly either the spin–orbit population ratios, or the observation that different rotational excitations are associated with each spin–orbit state.

B. NO state distributions from CID and photoinitiated unimolecular reactions

The detection biases discussed above, and the range of $E^{\dagger}$ involved in the CID experiments, make it hard to develop a quantitative model for the NO rotational distributions produced via CID. Nevertheless, a broad look is in order, and

comparisons between the CID and photodissociation results may be insightful, since in the latter, dissociation occurs via unimolecular reactions on S_0 and/or T_1 (see below). For example, if distributions obtained by the two methods differ significantly, the reaction mechanisms are surely different. However, if they are similar, the mechanisms might be the same.

The NO state distributions obtained in the CID experiments for both *n*- and *i*-C_3F_7NO throughout the range $3.0 < E_{incident} < 7.0$ eV, as well as at several T_s, can be characterized by temperature-like distributions for each spin–orbit state. Despite scatter and undulations, the distributions shown in Figs. 7–9 appear rather statistical, and depend weakly on $E_{incident}$ and T_s. The lower $^2\Pi_{1/2}$ spin–orbit state is more populous than $^2\Pi_{3/2}$, as has been observed in other unimolecular decompositions,[24] where we believe that NO spin–orbit populations are established late in the exit channel after nuclear motions such as NO rotation have developed. Figures 7 and 8 show that E_{rot} is consistently higher for $^2\Pi_{3/2}$ than $^2\Pi_{1/2}$, particularly at high J''. We note that this higher $^2\Pi_{3/2}$ rotational excitation could derive from $C_3F_7NO^\dagger$ having relatively high $E^\dagger$ values, since in the photodissociation experiments, $^2\Pi_{3/2}$ rotational distributions are nonstatistical at the higher $E^\dagger$, showing markedly increased high J'' populations.

In contrast to the CID experiments, molecules are prepared with single $E^\dagger$ values in the photodissociation experiments, and the measurements reflect the product state branching ratios. These can be well represented by prior distributions, implicating statistical unimolecular decomposition, except for the highest $E^\dagger$, where the onset of dynamical bias is observed (see Figs. 12 and 13). In exciting RNO molecules via the optically accessible S_1 state, fast, irreversible radiationless decay to S_0 and/or T_1 occurs (i.e., the fluorescence quantum yield is very small), and subsequent unimolecular reactions occur on T_1 and/or S_0.[24] In the photodissociation of C_3F_7NO, the rapid NO appearance times are compatible with dissociation on T_1 rather than S_0, since dissociation on S_0 is expected to proceed more slowly.[40] In fact, the *rise toward shorter wavelengths* of the NO yield spectrum observed with *n*-C_3F_7NO occurs as the absorption cross section is *dropping*, leading us to conclude that the $S_1 \rightarrow S_0$ and $S_1 \rightarrow T_1$ radiationless decay channels are competitive and essentially irreversible. Also, the NO quantum yield is much smaller than that obtained with CF_3NO, indicating that the major dissociation channel (presumably on S_0) is undetected at these photolysis wavelengths. We thus conclude that the *observed* NO in the photodissociation experiments derives from T_1, and this conclusion is supported by previous work on RNO molecules, which showed only a modest exit channel barrier for decomposition via T_1.[24,40]

The experimental observation time in the present photodissociation experiments was limited to 1 μs, discriminating strongly against reaction on S_0, which can be detected only at longer observation times. However, reaction via S_0 would also be expected to produce statistical or near-statistical NO state distributions, since there is no exit barrier for this channel.[24] As with previous studies, the lower spin–orbit state is overpopulated relative to statistical predictions.[24] We also identified an additional, nonstatistical channel at $E^\dagger > 3000$ cm^{-1} yielding NO($^2\Pi_{3/2}$) with high rotational excitation (Figs. 12 and 13). The process responsible for this channel is presently unknown, but may involve direct dissociation on S_1 above a barrier.

Figure 14 shows a comparison between typical rotational distributions obtained in the CID and photodissociation experiments. The similarity is striking; rotational distributions obtained via CID look similar to those obtained in the photodissociation of C_3F_7NO with $E^\dagger = 2000$–3000 cm^{-1}. Such similarities suggest that CID may occur from T_1 and/or S_0 via unimolecular decomposition at modest $E^\dagger$ values. Note, however, that for a molecule with many vibrational degrees of freedom (e.g., 30 for C_3F_7NO), the rotational populations are not very sensitive measures of $E^\dagger$ (see Figs. 12 and 13), so comparisons between the CID and photodissociation results can indicate only broad similarities. Although the CID experiments measure fragment densities that derive from a range of $E^\dagger$ values, it appears that there is no need to invoke mechanisms other than unimolecular decomposition via the lowest energy PES's that correlate adiabatically to products with little or no exit channel barriers. The NO yield in the photodissociation experiments is small, indicating that $S_1 \rightarrow S_0$ is more favorable than $S_1 \rightarrow T_1$. Thus, for T_1 to be the dominant participant in the CID experiments, it would have to be accessed more efficiently at comparable $E^\dagger$ values than in the photodissociation experiments, where T_1 is populated by ISC via S_1. However, in the CID experiments, reaction products are collected for a longer period of time than in the photolysis experiments, so reac-

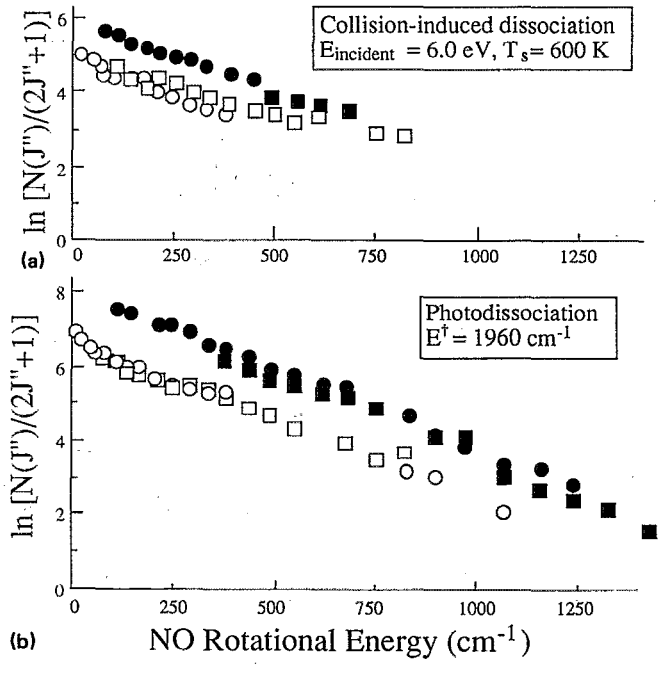

FIG. 14. Comparison between NO distributions obtained from *n*-C_3F_7NO using (a) CID at $E_{incident} = 6.0$ eV and (b) photodissociation at $E^\dagger = 1960$ cm^{-1}. Note the similarity between (a) and (b). The filled and empty symbols indicate rotational populations of $^2\Pi_{1/2}$ and $^2\Pi_{3/2}$ NO spin–orbit states, respectively.

tions occurring on S_0 will make larger relative contributions. Although it is natural to assume that vibrational excitation on S_0 is mainly responsible for the NO signals in the CID experiments, T_1 excitation resulting from collision-induced curve crossing cannot be precluded. Since the detection efficiency for NO deriving from the fast dissociation on T_1 is higher than for the S_0 reaction, *both* T_1 and S_0 may contribute to the observed NO CID yield.

C. Mechanisms and models

CID is one of the outcomes of molecule–surface collision-induced excitation, where we monitor only the subset with $E_{\text{internal}} > D_0$. The questions that should be asked therefore are of a general and fundamental nature: (i) What is the efficiency of the collisional excitation process, and how does it depend on the nature of the colliding molecule and the surface? (ii) How does the average internal energy and the shape of the $E^{\dagger}$ distribution depend on E_{incident} and T_s? (iii) What is the fraction of the excited molecules that dissociate, and which electronic states participate in the dissociation? (iv) What is the nature of the coupling to the surface?

At present, our knowledge is scant, and analogies with gas-phase collisional activation processes are not overly insightful, owing to the limited detailed microscopic information available about these processes. In the gaseous phase, CID has been studied in a number of systems that involve collisions of molecular ions at variable collision energies. Efficient conversion of translational to internal energy has been observed, with essentially complete dissociation occurring at c.m. collision energies of only a few eV.[14] Almost without exception, reactions follow low-energy dissociation pathways.[15] Similarly, the present data also point to an activation mechanism that involves coupling between E_{incident} and C_3F_7NO and MgO vibrations during the rather severe molecule–surface impact.

Some ideas regarding the widths and shapes of the E_{internal} distributions can be obtained from the dependences of the NO rotational distributions and CID yields on T_s. Our preliminary results show that although NO rotational excitation varies only weakly with T_s, the CID yield rises significantly. This suggests a broad E_{internal} distribution, whose width depends on T_s and E_{incident} in such a way as to yield, in all cases, the highest relative NO densities from molecules having $E^{\dagger}$ near D_0. We emphasize again, however, that NO rotational distributions are less sensitive to changes in $E^{\dagger}$ than are the CID yields. The efficiency of collision-induced excitation and the shape of the E_{internal} distribution may depend also on the parent molecule. For example, we did not observe CID for CF_3NO at $E_{\text{incident}} = 3.6$ eV and $T_s = 600$ K ($D_0 = 1.73$ eV). Under the same conditions, a significant signal, corresponding to $\sim 1\%$ yield, was obtained with C_3F_7NO. This places an upper limit of 0.1% on the CF_3NO CID yield at $E_{\text{incident}} = 3.6$ eV, indicating less efficient CID than for C_3F_7NO. Similar dependence on the colliding molecule was observed in the CID of a series of alkyl iodides.[13] Clearly, in addition to the state-resolved measurements described here, more work with different molecules and surfaces, and with angular and TOF resolution is needed in order to help unravel mechanisms.

V. SUMMARY

Consequent to the above arguments and considerations, the following list summarizes our present knowledge and findings.

C_3F_7NO molecules that have been expansion cooled and accelerated to fairly monoenergetic values of E_{incident} [i.e., $\Delta E_{\text{incident}}\,(\text{FWHM}) \sim 0.1\ E_{\text{incident}}$] collide with a MgO(100) surface under UHV conditions. The scattering is direct inelastic, as evidenced by the experimental observations.

Some of the rebounding molecules have $E_{\text{internal}} > D_0$, and CID is verified unambiguously by detecting NO state selectively using two-photon, two-frequency ionization. CID yields rise sharply with E_{incident}, with a value of $\sim 5\%$ at 6 eV ($D_0 \simeq 1.7$ eV). NO rotational distributions are temperature-like and reminiscent of statistical unimolecular decomposition.

Of the three potential surfaces that are energetically available in most of the CID experiments (S_0, T_1, S_1), dissociation can occur via the first two. S_1 usually has a large exit channel barrier, and is known to undergo rapid nonradiative decay to T_1 and/or S_0. Based on similarities with the present photodissociation results, as well as other photoinitiated unimolecular reactions on S_0 and/or T_1,[24] we conclude that CID is compatible with dissociation mainly on T_1 and/or S_0, with little or no exit channel barrier.

The CID technique described herein is general and can lead to significant dissociation probabilities at modest values of E_{incident}. Preliminary measurements indicate that the dissociation efficiency of C_3F_7NO increases with T_s, particularly for E_{incident} values near D_0, underscoring the utility of the method for energizing polyatomics above D_0 in order to examine dissociation pathways and mechanisms.

Although the present results can be rationalized by a statistical dissociation mechanism, there presently exists no proven model, and further experiments are clearly needed. Thus, we cannot rule out contributions from nonstatistical dissociation channels. Future experiments will involve (i) exciting incident molecules such as C_6F_5NO and NCNO to energies below D_0 using radiationless decay following $S_1 \leftarrow S_0$ optical excitation, (ii) studying T_s dependences, particularly near threshold, (iii) varying the nature of the surface, and most importantly, (iv) *exploiting* the technique for the purposes of studying single-collision, impact-induced decomposition of polyatomics.

ACKNOWLEDGMENTS

The authors thank R. B. Gerber, D. Baugh, J. Pfab, and A. Amirav for stimulating and fruitful discussions, and R. E. Banks for providing all of the C_3F_7NO samples. We also thank the referee for several helpful suggestions. Research supported by AFOSR and ARO.

[1] A. Amirav, P. L. Trevor, M. J. Cardillo, C. Lim, and J. C. Tully, J. Chem. Phys. **87**, 1796 (1987).
[2] E. Kolodney, A. Amirav, R. Elber, and R. B. Gerber, Chem. Phys. Lett. **113**, 303 (1985).
[3] A. Amirav and M. J. Cardillo, Phys. Rev. Lett. **57**, 2299 (1986).

[4](a) S. M. Liu, W. E. Rodgers, and E. L. Knuth, J. Chem. Phys. **61**, 902 (1974); (b) M. E. M. Spruit, P. J. van den Hoek, E. W. Kuipers, F. H. Geuzebroek, and A. W. Kleyn, Surf. Sci. **214**, 591 (1989); (c) F. O. Goodman and H. Y. Wachman, *Dynamics of Gas–Surface Scattering* (Academic, New York, 1976).
[5]A. Amirav and M. J. Cardillo, Surf. Sci. **198**, 192 (1988).
[6]M. C. Lin and G. Ertl, Annu. Rev. Phys. Chem. **37**, 587 (1986).
[7](a) A. W. Kleyn, A. C. Luntz, and D. J. Auerbach, Phys. Rev. Lett. **47**, 1169 (1981); (b) Surf. Sci. **117**, 33 (1982).
[8]G. D. Kubiak, J. E. Hurst, H. G. Rennagel, G. M. McClelland, and R. N. Zare, J. Chem. Phys. **79**, 5163 (1983).
[9]E. Kolodney, D. Baugh, P. S. Powers, H. Reisler, and C. Wittig, Chem. Phys. Lett. **145**, 177 (1988).
[10](a) G. O. Sitz, A. C. Kummel, and R. N. Zare, J. Chem. Phys. **89**, 2558 (1988); (b) **89**, 2572 (1988).
[11](a) C. T. Rettner, F. Fabre, J. Kimman, and D. J. Auerbach, Phys. Rev. Lett. **55**, 1904 (1985); (b) C. T. Rettner, J. Kimman, F. Fabre, D. J. Auerbach, and H. Morawitz, Surf. Sci. **192**, 107 (1987).
[12]A. C. Luntz, A. W. Kleyn, and D. J. Auerbach, J. Chem. Phys. **76**, 737 (1982).
[13]A. Danon, E. Kolodney, and A. Amirav, Surf. Sci. **193**, 132 (1988), and references cited therein.
[14](a) R. A. Yost and C. G. Enke, J. Am. Chem. Soc. **100**, 2274 (1978); (b) Anal. Chem. **51**, 1251 (1979).
[15](a) D. J. Douglas, J. Phys. Chem. **86**, 185 (1982); (b) S. E. Haywood, L. D. Doverspike, R. L. Champion, E. Herbst, B. K. Annis, and S. Datz, J. Chem. Phys. **74**, 2845 (1981).
[16]E. Kolodney and A. Amirav, in *Dynamics on Surfaces*, edited by B. Pullman, J. Jortner, A. Nitzan, and B. Gerber (Reidel, Dordrecht, 1984), Vol. 17, p. 231.
[17](a) E. Kolodney, A. Amirav, R. Elber, and R. B. Gerber, Chem. Phys. Lett. **111**, 366 (1984); (b) R. B. Gerber and A. Amirav, J. Phys. Chem. **90**, 4483 (1986).
[18]A. Danon and A. Amirav, J. Phys. Chem. **93**, 5549 (1989).
[19]A. Danon, A. Amirav, J. Silberstein, I. Salman, and R. D. Levine, J. Phys. Chem. **93**, 49 (1989).
[20](a) J. W. Gadzuk and S. Holloway, J. Chem. Phys. **84**, 3502 (1986); (b) J. W. Gadzuk and S. Holloway, Chem. Phys. Lett. **114**, 314 (1985); (c) S. Holloway and J. W. Gadzuk, Surf. Sci. **152**, 838 (1985).
[21]F. J. Bottari and E. F. Greene, J. Phys. Chem. **88**, 4238 (1984).
[22]J. D. Beckerle, A. D. Johnson, Q. Y. Yang, and S. T. Ceyer, J. Chem. Phys. **91**, 5756 (1989).
[23]A preliminary report is given in E. Kolodney, D. Baugh, P. S. Powers, H. Reisler, and C. Wittig, J. Chem. Phys. **90**, 3883 (1989).
[24]H. Reisler, M. Noble, and C. Wittig, in *Molecular Photodissociation Dynamics*, edited by J. Baggott and M. N. R. Ashfold (Royal Society of Chemistry, London, 1987).
[25]K. H. Rieder, Surf. Sci. **118**, 57 (1982).
[26]E. Kolodney and A. Amirav, Surf. Sci. **155**, 715 (1985).
[27](a) J. C. Miller and R. N. Compton, Chem. Phys. Lett. **93**, 453 (1982); (b) F. Lahmani, C. Lardeux, D. Solgadi, A. Zehnacker, I. Dimicoli, M. Boivineau, M. Mons, and F. Piuzzi, J. Phys. Chem. **89**, 5646 (1985); (c) J. C. Miller and R. N. Compton, J. Chem. Phys. **75**, 22 (1981).
[28](a) J. Mason, J. Chem. Soc. **1957**, 3904; (b) *The Chemistry of Nitro and Nitroso Groups*, Part I, edited by H. Feuer (Interscience, New York, 1969); (c) J. G. Calvert and J. N. Pitts, Jr., *Photochemistry* (Wiley, New York, 1967).
[29]L. T. Earles, Phys. Rev. **48**, 423 (1935).
[30](a) J. B. Fenn, Entropie **18**, 11 (1967); (b) N. Abuaf, J. B. Anderson, R. P. Andres, J. B. Fenn, and D. R. Miller, in *Rarefied Gas Dynamics Vol. 5*, (Academic, New York, 1967), p. 1317.
[31]E. Kolodney and A. Amirav, Chem. Phys. **82**, 269 (1983).
[32]Y. Y. Bai, A. Ogai, C. X. W. Qian, L. Iwata, G. A. Segal, and H. Reisler, J. Chem. Phys. **90**, 3903 (1989).
[33]M. H. Alexander *et al.*, J. Chem. Phys. **89**, 1749 (1988).
[34]D. Burgess, Jr., R. R. Cavanagh, and D. S. King, J. Chem. Phys. **88**, 6556 (1988).
[35]S. A. Buntin, L. J. Richter, D. S. King, and R. R. Cavanagh, J. Chem. Phys. **91**, 6429 (1989).
[36]B. M. Smirnov, *Negative Ions* (McGraw-Hill, New York, 1982).
[37]R. D. Levine and R. B. Bernstein, *Molecular Reaction Dynamics* (Oxford University, Oxford 1987).
[38](a) *Atomic and Molecular Beam Methods*, edited by G. Scoles (Oxford University, Oxford, 1988), Vol. I; (b) J. F. de la Mora and J. Rossell-Llompart, J. Chem. Phys. **91**, 2603 (1989).
[39](a) R. Butler and A. Snelson, J. Fluorine Chem. **16**, 33 (1980); (b) D. A. C. Compton and D. M. Rayner, J. Phys. Chem. **86**, 1633 (1982).
[40]P. J. Robinson and K. A. Holbrook, *Unimolecular Reactions* (Wiley–Interscience, New York, 1972).
[41]M. Noble, C. X. W. Qian, H. Reisler, and C. Wittig, J. Chem. Phys. **85**, 5763 (1986).
[42]Accurate unimolecular reaction rates could not be calculated because they are very sensitive to unknown transition state parameters.
[43]R. D. Bower, R. W. Jones, and P. L. Houston, J. Chem. Phys. **79**, 2799 (1983).
[44]*American Institute of Physics Handbook*, 3rd ed. (McGraw-Hill, New York, 1982).
[45]E. Kolodney, P. S. Powers, L. Iwata, H. Reisler, and C. Wittig (unpublished).
[46]G. Vidali and D. R. Frankel, Phys. Rev. B **27**, 2480 (1983).